AIP | Journal of Applied Physics

Surface acoustic wave velocity of gold films deposited on silicon substrates at different temperatures

E. Salas, R. J. Jiménez Riobóo, C. Prieto, and A. G. Every

Citation: J. Appl. Phys. **110**, 023503 (2011); doi: 10.1063/1.3606412
View online: http://dx.doi.org/10.1063/1.3606412
View Table of Contents: http://jap.aip.org/resource/1/JAPIAU/v110/i2
Published by the American Institute of Physics.

Surface acoustic wave velocity of gold films deposited on silicon substrates at different temperatures

E. Salas,[1,a)] R. J. Jiménez Riobóo,[1] C. Prieto,[1] and A. G. Every[2]
[1]*Instituto de Ciencia de Materiales de Madrid, Consejo Superior de Investigaciones Científicas, Cantoblanco, Madrid 28049, Spain*
[2]*School of Physics, University of the Witwatersrand, Wits 2050, South Africa*

(Received 4 February 2011; accepted 26 May 2011; published online 19 July 2011)

Au thin films have been deposited by DC magnetron sputtering on Si (001) substrates at different substrate temperatures, ranging from 200 K to 450 K. With increasing temperature, the expected crystallinity and morphology of the Au thin film are clearly improved, as shown by x ray diffraction, atomic force microscopy and scanning electron microscopy experiments. Parallel to this, the surface acoustic wave propagation velocity shows a clear enhancement toward the ideal values obtained from numerical simulations of a Au thin film on Si (001) substrate. Moreover, a very thin and slightly rough interlayer between the Si (001) substrate and the Au thin film is developed for temperatures above 350 K. The composition and nature of this interlayer is not known. This interlayer may be responsible for the steep change in the structural and elastic properties of the Au thin films at the higher temperatures and possibly also for an improvement of the adhesion properties of the Au on the Si (001) substrate. © *2011 American Institute of Physics*.
[doi:10.1063/1.3606412]

I. INTRODUCTION

The properties of gold thin films have been extensively studied for their numerous applications in mechanical, optical, biological, and magnetic devices. Recently, Au films have been used as interlayers in spin-valve structures,[1] as functional components in micro/nano-electro-mechanical systems (MEMS/NEMS),[2] and as catalytic elements in biological applications. MEMS devices combine mechanical and electrical effects in their application to new technologies, like micro fuel cells.[3] Materials with high thermal conductivity and stability[4,5] are being developed to be used in MEMS and NEMS devices to provide special functionalities. In all these applications, the contact properties between noble metals and Si substrates are of crucial importance, and the tendency of metal diffusion into the Si substrate has to be taken into account. In view of this, deposition temperature would appear to be a relevant parameter that influences the behavior of the metal-silicon system.[6–10]

Typical deposition techniques that have been used to grow Au thin films are pulse laser deposition (PLD)[11] and electroless deposition,[12] or sputtering. In the case of the sputtering technique, typically, polycrystalline films are obtained with face centered cubic (*fcc*) (111) texture perpendicular to the film plane,[13] where grain size determines its functionality. For that reason, several after grown processes, such as ion irradiation[14] and annealing, can be used to change the initial properties of gold films after deposition. On the other hand, improvement of mechanical properties and film adhesion to the substrate has been checked by gold alloying with other metals, such as Cr or V.[15] Nevertheless, to our knowledge, the influence of the substrate temperature during deposition on the elastic properties of gold thin films deposited by sputtering on silicon has not been reported.

The elastic properties of gold thin films on different substrates have been already investigated in order to find out whether the bulk properties are maintained or not in the thin film form.[16–18] Results provide a gold thin film shear elastic constant value that is clearly lower (at least 10%) than the corresponding one for the bulk. But for gold alloys films,[19] no studies dealing with thin films elastic anisotropy have been reported.

On the other hand, film growing at different substrate temperatures by magnetron sputtering, especially below room temperature, has been reported to influence macroscopic quantities, such as elastic properties of carbon layers[20] and microscopic properties, such as grain size of iron films.[21,22] In this sense, grain size and oxidation degree have been used to explain the elastic properties that are responsible for the observed surface acoustic waves (SAW) velocity of iron thin films.[23]

Regarding gold thin films, annealing processes have been typically conducted in the study of properties modification; variations of electrical conductivity,[24] structural,[25] and mechanical[26] properties have been studied in Au thin films using post-deposition annealing techniques. However, the properties of gold thin films deposited at low temperatures have scarcely been studied.[27] On the other hand, and as said above, to improve adhesion of gold films to the substrate, a buffer layer is usually deposited, but no attention has been paid to the behavior of the Au-Si interface when depositing at different temperatures and its influence on the properties of the Au thin films.

The aim of this work is to elucidate whether the growth of gold thin films on Si (001) substrates deposited by DC

a)Author to whom correspondence should be addressed. Electronic mail: esalas@icmm.csic.es.

magnetron sputtering at different substrate temperatures influences the elastic properties of the gold thin films. To study the elastic properties, SAW velocity has been characterized by high resolution Brillouin spectroscopy (HRBS). The observed variation is explained in terms of crystallinity, morphology, and surface elastic properties, as well as interface between thin film and Si substrate. For that purpose, microstructural and morphological characterizations have been performed by x ray reflectivity (XRR), x ray diffraction (XRD), atomic force microscopy (AFM), and scanning electron microscopy (SEM) techniques, which have proven to be appropriate to characterize Au films.[28]

II. EXPERIMENTAL

Au thin films were deposited by DC magnetron sputtering on Si (001) substrates at different substrate temperatures from a 99.95% pure gold sputtering target. A 2 inches planar magnetron was used for this purpose with an Ar pressure of 5×10^{-3} mbar and a base pressure in the 10^{-7} mbar range. A power of 10 W was applied to obtain a deposition rate of 3.2 nm/min. Substrate temperature was selected from 200 K to 450 K by using a home modified cold finger Oxford CF-100 continuous flow cryostat. The cryostat was managed by an Oxford ITC-502 temperature controller, which allows controlling temperatures with a precision better than 1 K.

Thickness and crystallinity of the samples were studied by x ray reflectivity (XRR) and x ray diffraction (XRD) in a Bruker AXS D8 DISCOVER 4-axis diffractometer at the Bragg-Brentano configuration, with the Cu K_α emission line. The x ray diffractometer is equipped with a Göbel mirror (to collimate the x ray beam), a 4 bounce Ge (220) monochromator (to filter Cu $K_{\alpha 1}$ emission line), and an automatic rotary absorber from the x ray generator to the sample holder. Further, a scintillator detector, through a pathfinder with a selectable divergence slit from 3.0° to 0.1°, was used.

Surface topography of the Au thin films was studied via AFM and SEM experiments. AFM images were collected using a commercial head and software from Nanotec™.[29] Commercial Nanosensors PPP-NCH-w tips, with $k = 42$ Nm^{-1} and $f_0 = 330$ kHz, were used for topographic characterization using the contact mode.

SEM images were taken with a FE-SEM FEI Nova NANOSEM 230 microscope. The electron beam was produced by a high-stability Schottky field emission gun with a voltage of 8 kV. A low-voltage high-contrast detector vCD, paired with beam deceleration, was used for detection. This detector allows taking film topography by applying low voltage.

Surface acoustic waves (SAW) and elastic properties of Au samples were studied by high resolution Brillouin spectroscopy.[30] The experiment was carried out in backscattering geometry[31] with a 2060 Beamlok Spectra Physics Ar-ion single mode laser, $\lambda = 514.5$ nm, as monochromatic light source and a tandem 3 + 3-Pass Fabry-Pérot interferometer as Brillouin spectrometer.[32] The incoming light is polarized in the scattering plane in order to couple the acoustic wave vector (k) with the surface acoustic wave.[33] In this way, SAW velocity is defined as $v_{SAW} = \omega/k$, where ω is $2\pi f$ (f is the Brillouin frequency shift), $k = 4\pi/\lambda(\sin\theta_s)$ is the acoustic wave vector involved, λ is the laser wavelength in vacuum, and θ_s is the incident sagittal angle from the normal.

In addition, numerical simulations[34] have been carried out in order to compare with experimental data. Elastic constants used in the numerical simulations are listed in Table I.

III. RESULTS AND DISCUSSION

The evolution of the XRR, corresponding to samples prepared at different substrate temperature, is shown in Fig. 1. These curves are used to obtain fairly precise values of Au thin film thickness grown on the Si (001) substrate, which are also given in Fig. 1.

As it can be seen in Fig. 1, the number of finite size related detected maxima (Kiessig fringes) diminishes with increasing substrate temperature; additionally, above room temperature (RT) wide maxima begin to develop. Those wide maxima suggest some ordering at the interface (interlayer formation) induced by deposition at temperatures higher than RT.

The loss of finite size narrow maxima at high angles when increasing substrate temperature can be explained by a roughness increase at the Au/Si (001) interface as well as at

TABLE I. Summary of elastic constants for Si and for different Au symmetries and spatial averages taken into account in the numerical simulations. V, R, and H stand for Voigt, Reuss, and Hill averages, respectively.

Compound		Density (g/cm^3)	c_{11} (GPa)	c_{12} (GPa)	c_{13} (GPa)	c_{33} (GPa)	c_{44} (GPa)	c_{66} (GPa)	c_{14} (GPa)
Au cubic matrix (Ref. 39)		19.30	186	157			42		
Au polycrystalline (isotropic) (Ref. 39)		19.30	207.0	150.0			28.5		
Si (001) substrate (Ref. 39)		2.33	165.6	63.9			79.5		
Native SiO_2 interlayer (Ref. 39)		2.2	78.5				31.2		
Gold isotropic	Voigt average	19.30	208.00				31.00		
	Reuss average	19.30	198.50				23.88		
	Hill average	19.30	203.25				27.44		
Au <111> trigonal		19.30	213.50	147.83	138.67	222.67	23.67	32.83	12.96
Au <111> (average in the basal plane)	Voigt	19.30	213.50	147.83	138.67	222.67	23.67	32.83	0
	Reuss	19.30	206.40	154.93	138.67	222.67	18.55	25.73	0
	Hill	19.30	209.95	151.38	138.67	222.67	21.11	29.28	0

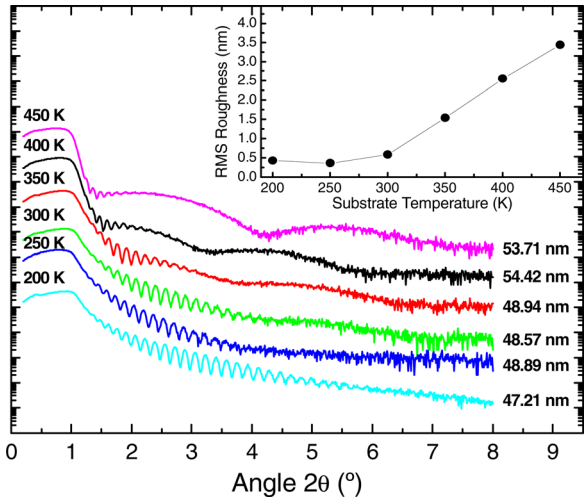

FIG. 1. (Color online) XRR patterns of Au samples deposited at different substrate temperatures. Interference peaks observed are employed to obtain thickness using Bragg's Law. Arbitrary units were taken and spectra were vertically shifted for the sake of clarity.

the surface of Au films. Probably, a combination of both effects is affecting the XRR results.

X ray diffraction experiments have been carried out in order to study the microstructural properties of Au thin films; the corresponding (111) diffraction peaks belonging to the Au *fcc* structure are shown in Fig. 2. Samples show also a high degree of texture, as it has been confirmed by the rocking curves given in the inset of Fig. 2. The width analysis of the (111) peak gives an estimation of the grain size through the determination of the length of coherence by the Scherrer formula.

The experimental specular configuration implies that the information on the grain size has to be taken as a measure of the average grain size along the direction perpendicular to the film plane.[35] On the other hand, as expected, no information regarding the interlayer could be obtained.

The sample grown at 450 K presents better (111) texture and bigger size of the Au grains (narrower (111) diffraction peak), as shown by x ray diffraction. It is known that increasing substrate temperature influences the microstructure[21] and, thus, it is difficult to infer the real influence of the existence of an interlayer on the crystallinity and morphology of the Au thin films.

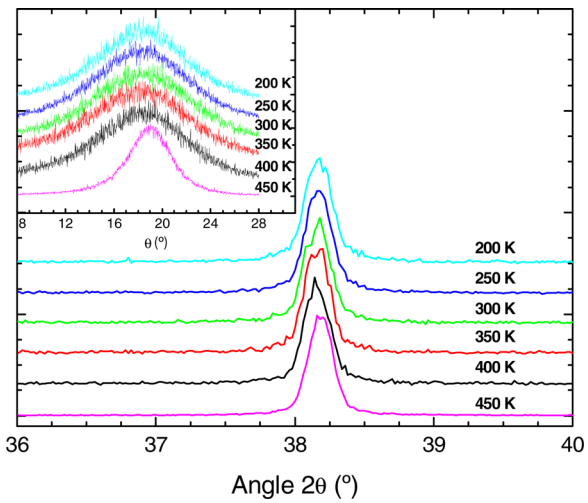

FIG. 2. (Color online) XRD patterns showing the (111) diffraction peak of the Au samples. Inset, rocking curves in the ⟨111⟩ direction. Arbitrary units were taken and spectra were vertically shifted for the sake of clarity.

Figure 3 presents the AFM images for three samples deposited at 200 K, 300 K, and 450 K, respectively. Clear changes in topography can be observed by the naked eye. At

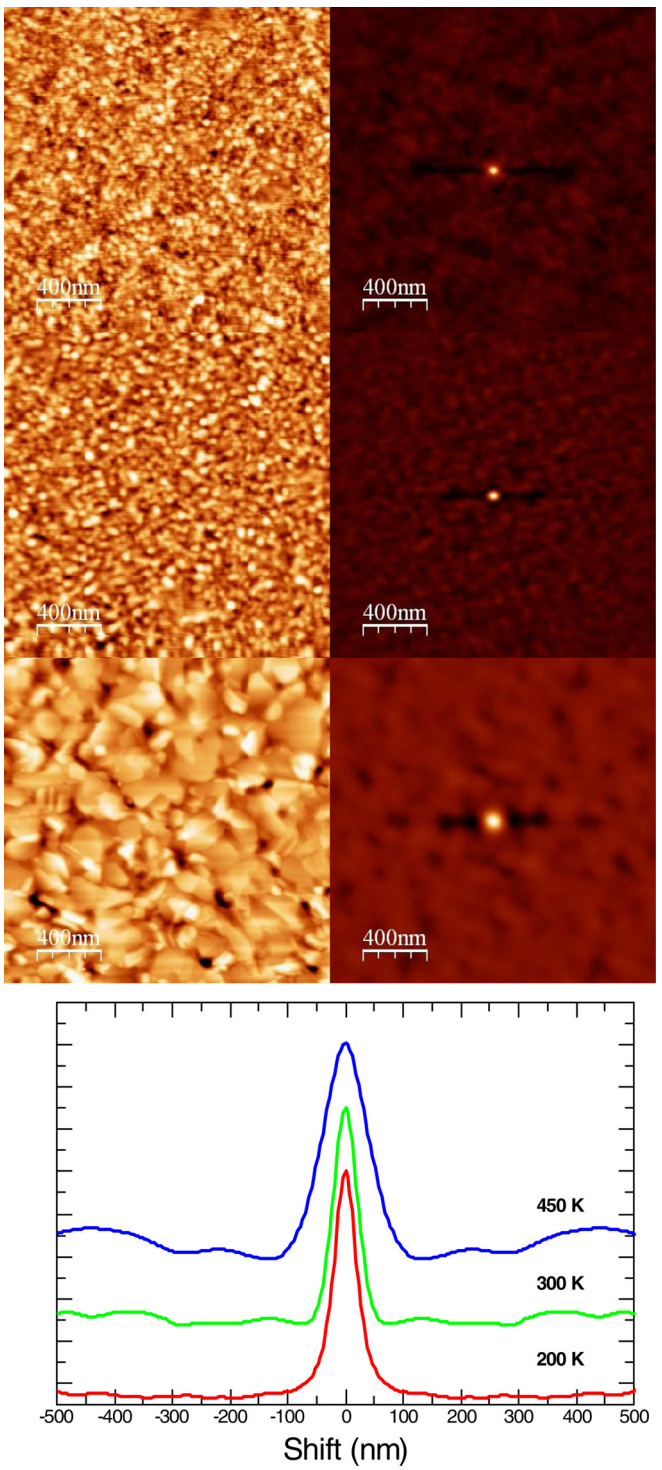

FIG. 3. (Color online) 2×2 μm AFM contact mode pictures of Au thin films deposited at 200 K (up), 300 K (center), and 450 K (down) are shown in the first column, with their respective self-correlation pictures in the second column. The intensity profiles obtained by means of self-correlation images at horizontal-central line are plotted under the pictures.

higher temperatures, the grain size increases. An average of the grain size in the directions contained in the film plane of the samples has been calculated using the AFM images and using the self-correlation procedure. This method evaluates the integral of the convolution of the image, multiplied by itself, shifted a distance in both axes. A self correlation image is defined as

$$G(k_1, k_2) = \sum f(x, y) f(x + k_1, y + k_2), \qquad (1)$$

where $f(x, y)$ is the AFM image and k_1 and k_2 are the shifted distances in the X and Y axis with respect to the center of the image. This function gives information of the average "in-plane" grain size from the full width at half maximum (FWHM) of the peak obtained in the self-correlation image.[36]

AFM measurements can give valuable information about film surface roughness. The temperature evolution of roughness (rms) is plotted in the inset of Fig. 1 to compare more easily with the XRR temperature evolution. Surface roughness does not show any relevant change until 300 K. Above this temperature, the roughness increases from 0.5 nm (that is typically the measured value for Si substrate) up to about 3.5 nm for samples prepared at 450 K.

XRR and AFM results can be interpreted in the way that the Au/Si (001) interface becomes rougher with increasing temperature and develops an interlayer. This fact is in accordance with the registered new features (wide maxima in XRR). Moreover, the loss of narrow maxima, especially at temperatures above 300 K, must be due to a loss in local parallelism between film surface and film/substrate interface that can be induced by a combination of the increase of film surface roughness and the development of a new interlayer, which may also present rough interfaces. A rough estimation of the interlayer thickness (from the wide maxima) gives 3.2 nm for the sample prepared at 450 K. This thickness value is very similar to the value obtained for the native SiO_2 layer of the Si (001) wafers by means of spectroscopic ellipsometry. The presence of the native SiO_2 layer can be detected by the XRR as a modulation of the Kiessig fringes' pattern and is clearly seen in the sample grown at 200 K. Therefore, the interlayer detected at temperatures above 350 K must be different to the native SiO_2 layer.

Figure 4 shows SEM pictures of samples deposited at 200 K, 300 K, and 450 K. Differences in the film topography, depending on the substrate temperature, can be also observed in such a way that bigger grains are detected in samples deposited at higher temperatures. Both AFM and SEM give similar behavior for the average grain size in the directions contained in the film plane of samples.

In summary, it is very difficult to separate temperature effects from the effect of the interlayer on the structural properties of the Au thin films. Therefore, no special influence of the interlayer can be clearly isolated.

Even though it is not rare to find gold silicides or even Au-Si alloys that may form an interlayer at the interface between the Au thin film and the Si substrate, as already reported in the literature,[6,9,10] no information concerning the nature of the interlayer detected in the above presented measurements was obtained.

In order to study the elastic properties of gold thin films, HRBS has been used. Being aware of the influence of the Si (001) substrate on the elastic properties of the films investigated, the sagittal angle was carefully fixed so that the product $k \times h$ was accurately known, k being the surface acoustic wave vector and h the film thickness after taking into

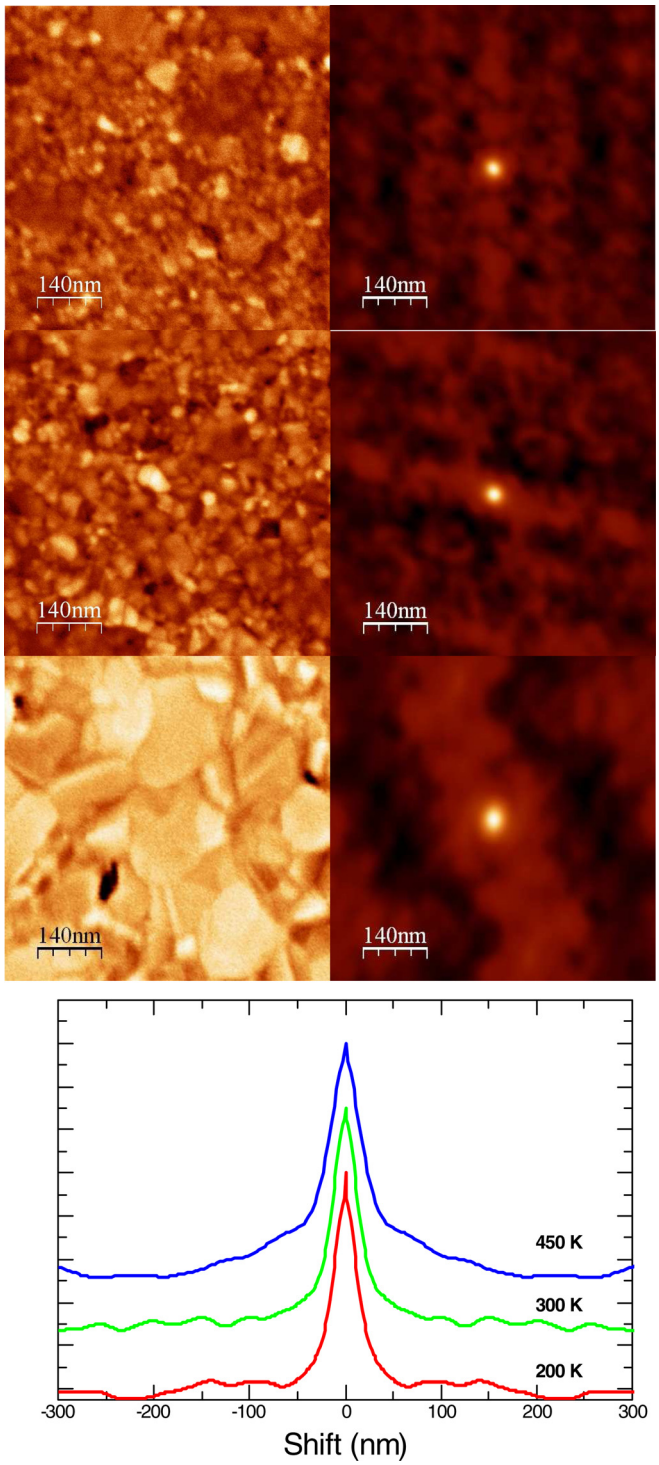

FIG. 4. (Color online) 700 × 700 nm SEM pictures of the surface of Au thin films deposited at 200 K (up), 300 K (center), and 450 K (down) are shown in the first column, with their respective self-correlation pictures in the second column. The intensity profiles obtained by means of self-correlation images at horizontal-central line are plotted under the pictures.

account the film thickness precisely measured by XRR. Then, samples were rotated around the normal to the film plane (azimuthal angle) to study the angular dependence of the SAW propagation velocity in the film plane. The scattering volume was placed off-center so that the direction and position of the acoustic wave vector changed, making possible the simultaneous testing of the sample homogeneity and elastic symmetry (Fig. 5(a)).

Figure 5(b) shows a typical HRBS spectrum in which Rayleigh and Sezawa peaks are clearly observed. In as far as the Rayleigh-SAW is the most intense surface vibrational mode, our attention was focused on this Rayleigh-SAW and the dependence of its propagation velocity (v^R) on the substrate temperature during the growing process.

Figure 6 gives the experimental Rayleigh velocity values as a function of the azimuthal angle for all studied samples, where the origin of angles has been selected in coincidence with the <100> crystallographic direction of Si (001) substrate. Two facts can be observed; first, a periodic behavior (of weak amplitude), as expected from a very thin film deposited on a single crystal substrate, and second, a clear evolution of the SAW velocity as a function of the preparation substrate temperature.

The SAW velocity depends on several factors, the density and elastic moduli of the Si substrate, the gold film and the intermediate layer, and the thicknesses or rather the products $k \times h$ for the gold film and intermediate layer. In order to understand the influence of the deposition temperature on the surface dynamical behavior of the film-layer-substrate system, we have conducted extensive simulations of the HRBS spectrum, drawing on the data presented in Table I. In this table are listed the published measured values of the densities and elastic moduli of cubic crystal silicon and gold and of isotropic polycrystalline gold and SiO_2, as well as a number of sets of elastic moduli of polycrystalline gold calculated from the single crystal elastic constants on the basis of various idealised effective media assumptions. We assume here that the crystallites fill the space available, so that in all cases the density is that of crystalline gold, i.e., $\rho = 19.30$ g/cm^3, and there is no porosity or related effects influencing the elastic moduli.

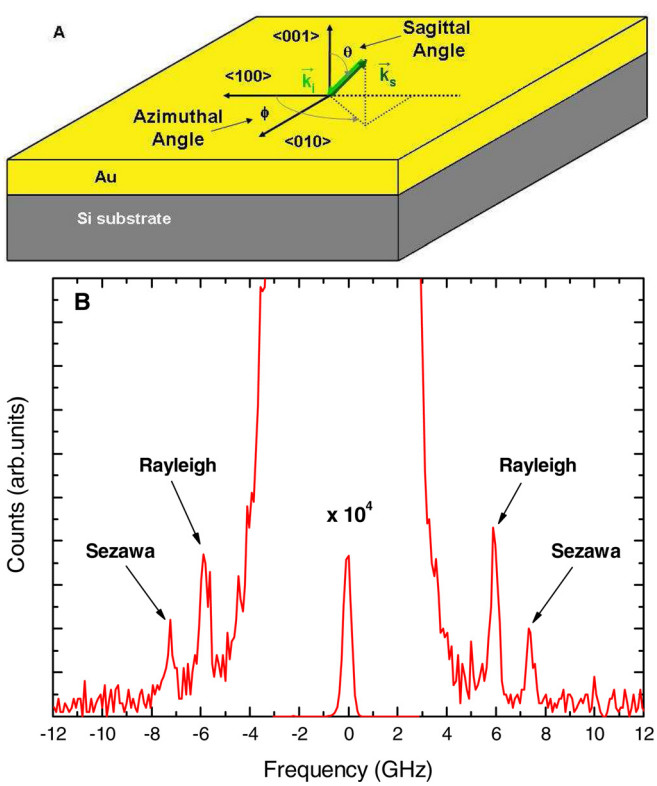

FIG. 5. (Color online) (a) Experimental configuration of HRBS on the Au samples deposited on Si (001) substrate. $\vec{k}_i$ represents the wave vector of the incident laser beam ($\lambda = 514.5$ nm), $\vec{k}_s$ represents the wave vector of the scattered light, ϕ is the azimuthal angle (defined $\phi = 0$ in direction $\langle 100 \rangle$) and θ is the sagittal angle (defined $\theta = 0$ in direction $\langle 00\text{-}1 \rangle$). (b) HBRS spectrum of sample prepared at 400 K and azimuthal angle of 110°. Rayleigh and Sezawa SAW peaks can be observed.

Polycrystalline media consisting of completely randomly oriented crystallites are elastically isotropic and possess only two independent elastic constants, which in the Voigt contracted notation are c_{11} and c_{44}, with $c_{12} = c_{11} - 2c_{44}$. The most common approaches to calculating these constants are the Voigt, Reuss, and Hill models. The Voigt model assumes the same uniform strain in all the crystallites, relates the stress field in each of the crystallites to the strain field via the rotated elastic modulus tensor, averages the stress field over all the crystallites, and then extracts the effective elastic constants from the relation between the average stress field and the strain field. This reduces to averaging the single crystal elastic modulus tensor rotated over all possible orientations of the coordinate axes. The Reuss model assumes a uniform stress field in all the crystallites, reduces to averaging the single crystal elastic compliance tensor rotated over all possible orientations of the coordinate axes, and involves inversion between the elastic moduli and compliance tensors at the start and end of the process. Both the Reuss and Voigt models are over idealised and also subject to certain thermodynamic reservations. The Hill model, which is not subject to these thermodynamic shortcomings and, moreover, tends to give much better agreement with measurement, yields elastic constants which are the averages of the Voigt and Reuss constants. Table I lists the Voigt, Reuss, and Hill elastic constants for isotropic polycrystalline gold, and it can be seen that the Hill values are in satisfactory agreement with the measured values.

The gold films we have been studying are, however, as has been clearly spelled out earlier, not isotropic but possess $\langle 111 \rangle$ texture normal to the Si surface, i.e., with all the crystallites having a $\langle 111 \rangle$ axis parallel to each other and oriented normal to the Si surface. Were the orthogonal axes of the crystallites also parallel to each other, which of course is not the case, then by taking the Cartesian x_3 axis along the $\langle 111 \rangle$ and the x_1 and x_2 along the two orthogonal directions, the rotated elastic constant matrix, as shown in Table I, has the appearance of that for trigonal $R1$ symmetry, with 6 independent elastic constants (the seventh constant $c_{66} = (c_{11} - c_{12})/2$). The textured film is, however, structured such that a $\langle 111 \rangle$ axis of the crystallites is normal to the substrate, but the orthogonal axes take on all possible orientations around that $\langle 111 \rangle$ with equal probability. There is thus no preferred axis normal to the $\langle 111 \rangle$ direction, and the medium thus

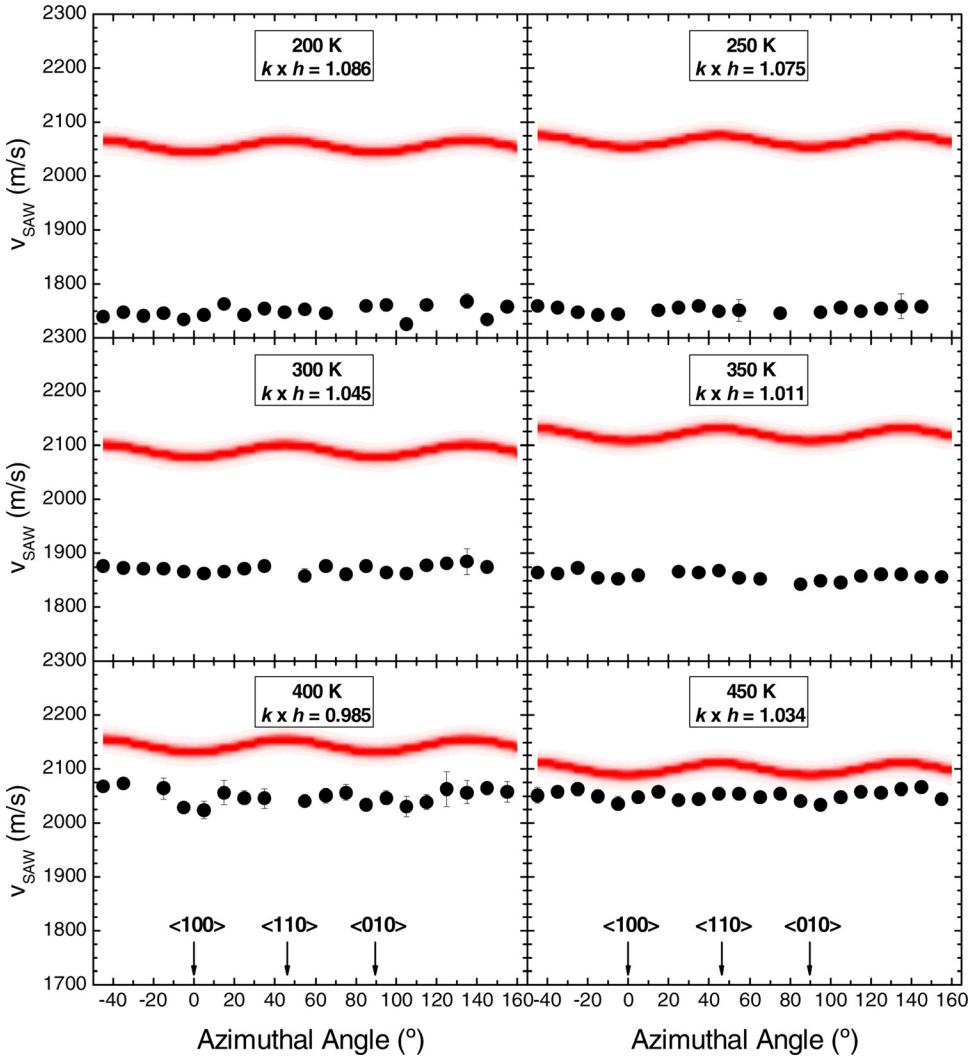

FIG. 6. (Color online) Comparison between SAW velocity (Rayleigh mode) experimental values of samples deposited at different substrate temperatures and numerical simulation of Au polycrystalline isotropic film (see values in Table I). Azimuthal angle 0° matches with direction ⟨100⟩ and 45° with ⟨110⟩ of Si (001) substrate.

possesses transverse isotropy with 5 independent elastic constants, c_{11}, c_{12}, c_{13}, c_{33}, and c_{44}, with $c_{66} = (c_{11} - c_{12})/2$ and $c_{14} = 0$. A thorough discussion on this point can be found in the Appendix. Table I lists the ⟨111⟩ textured averaged Voigt, Reuss, and Hill elastic constants of gold. It is interesting to note that, in the case of two of the constants, c_{13} and c_{33}, the Voigt and Reuss values are the same, a fact previously reported by Hendrix and Yu.[37] Bearing in mind the discussion of the previous paragraph, the expectation is that the Hill constants, obtained by averaging the Voigt and Reuss constants, are likely to be a better reflection of the actual constants of the gold film than either the Voigt or Reuss constants. The Hill constants have thus been the initial input into our simulations.

The numerical simulations (see Fig. 6) can be regarded as a SAW velocity upper limit in the case of a ⟨111⟩ textured Au thin film on a Si (001) substrate.

Several reasons have been adduced to justify the observed diminution of SAW velocities with respect to the theoretically calculated ones. For instance, some authors have proposed the "in-plane" grain size as the cause for this decrease.[16] Also, the existence of a thin native SiO_2 layer on top of the Si (001) must be taken into account.

The obtained difference between the experimental variation of the SAW velocity values and the numerical ones has been plotted in Fig. 7(a) versus the preparation substrate temperature. It should be noted that, since the SAW velocity has a periodic variation, the represented values correspond to the average over a 180° range of the azimuthal angle. For correlation purposes, microstructural properties obtained from XRD data and from AFM and SEM images are shown in Figs. 7(b) and 7(c). The average "out-of-plane" grain size has been obtained from the FWHM of Au (111) x ray diffraction peaks; its behavior does not show large differences between samples, giving typical values of one half of the film thickness and pointing toward bigger sizes for temperatures higher than 400 K. On the other hand, average "in-plane" grain sizes, obtained by the self-correlation of the AFM and SEM pictures, present a nearly monotonous increasing behavior with preparation temperature showing a similar behavior as those obtained for SAW velocities. The quantitative differences in the AFM and SEM data must not be over interpreted; both techniques show the same qualitative behavior. It should be taken into account that AFM is specially sensitive to "out-of-plane" displacements, which gives an excellent measure of roughness, but raw experimental "in-plane" measurements are convoluted

with the tip size, which can allow pictures larger than the actual grain size. From the experimental facts displayed in Fig. 7, it seems clear that, not only the temperature, but an additional influence must be taken into account in order to interpret the results above 350 K. This additional influence results in a steeper variation of structural parameters for the higher temperatures. At these temperatures, the existence of an interlayer different from the native SiO_2 one has been detected, and it could be the reason for this steeper variation.

Tanimoto *et al.*[25] have reported that the density of Au sputtered films grown at high substrate temperatures (340 K–390 K) is the same as the gold bulk one ($\rho = 19.283$ g/cm^3), while samples grown at lower temperatures present slightly lower values. This fact is in agreement with the microscopic evolution of crystalline size as a function of substrate temperature, where bigger crystallites provide higher densities.

SAW velocity values smaller than the here reported ones have been already observed in Au thin films grown on Si by Bassoli *et al.*,[38] as well as on glass substrates by Hildebrands *et al.*[16] In both of them, the bulk shear wave propagation velocities determined from the experimental SAW velocity values result to be very small ($v_T = 1125$ m/s from Ref. 38 and $v_T = 1075$ m/s from Ref. 16) when compared with the literature reported values for polycrystalline gold[39] ($v_T = 1215.2$ m/s). Authors of Refs. 16 and 38 have proposed a shear modulus bulk value of $c_{44} = 25$ GPa that is clearly lower than the literature values ascribed to polycrystalline gold, $c_{44} = 28.5$ GPa in Ref. 39 or $c_{44} = 27.71$ GPa in Ref. 40. Au thin films of Refs. 16 and 38 were grown at room temperature, and the authors were already aware of the possibility that the thin films could not reflect exactly the bulk elastic properties due to different physical reasons.

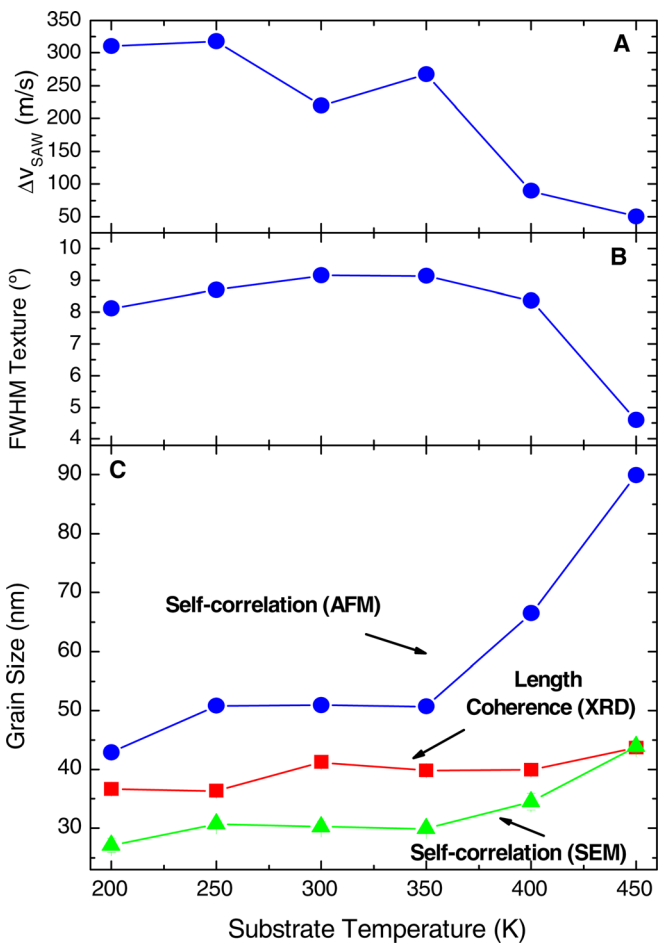

FIG. 7. (Color online) Comparison between the average SAW velocity (a) and microstructural experimental data as a function of the used substrate temperatures during deposition. FWHM texture (b) and length of coherence (c) values obtained from XRD patterns; surface grain size values from AFM and SEM are also plotted (c).

Thus, crystallite size, topography, and, to a lesser extent, densification may account for the diminution of the observed sound velocity values.

Assuming that the changes to the SAW velocity are mainly due to variations of elastic constants of the film, it is possible to extract the evolution of the elastic constants with the substrate temperature using numerical simulations of the SAW velocities. As a first approximation, the influence of the interlayer or of the SiO_2 native layer is neglected and all the elastic constants (5 independent constants) are allowed to change in the same proportion. In order to reproduce the experimental values of the Rayleigh SAW velocity, the simulations were performed using the ideal elastic constants (VRH; Table I) but reduced in a factor that is different for the different substrate temperatures. The final results are shown in Table II. As can be seen, the samples grown at higher temperatures present values of the elastic constants very near to the ideal ones.

The mean experimental values obtained for the Au thin film sample prepared at 450 K and the numerical simulation of the mean SAW propagation velocities obtained with the hexagonal VRH values of gold shown in Table I give 2050 m/s and 2100 m/s, respectively, (2.38% difference). In order to improve the description of the experimental data, an additional native SiO_2 interlayer (elastic constant values in Table I) of 3 nm thickness has been taken into account. The corresponding numerical simulation value of the system Au/SiO_2/Si (001) (2066 m/s) is 1.6% lower than the previous one with no native SiO_2 interlayer and is very near to the experimental value (2050 m/s). As it has been discussed above, not simply the native SiO_2 interlayer, but a somewhat more complex interlayer has been detected by XRR. The influence of a 3 nm layer containing different Au percentages within the native SiO_2 on the Rayleigh-SAW velocity can be also simulated. Figure 8 shows the dependence obtained in the case of the sample grown at 450 K. The Au was considered as

TABLE II. Evolution of the 5 independent elastic constants of <111> textured gold with the substrate temperature.

Temperature (K)	Factor	c_{11} (GPa)	c_{12} (GPa)	c_{13} (GPa)	c_{33} (GPa)	c_{44} (GPa)
200	0.415	87.13	62.82	57.55	92.40	8.76
250	0.410	86.08	62.07	56.85	91.29	8.66
300	0.485	101.83	73.42	67.25	107.99	10.24
350	0.435	91.33	65.85	60.32	96.86	9.18
400	0.710	149.06	107.48	98.46	158.09	14.99
450	0.840	176.36	127.16	116.48	187.03	17.73

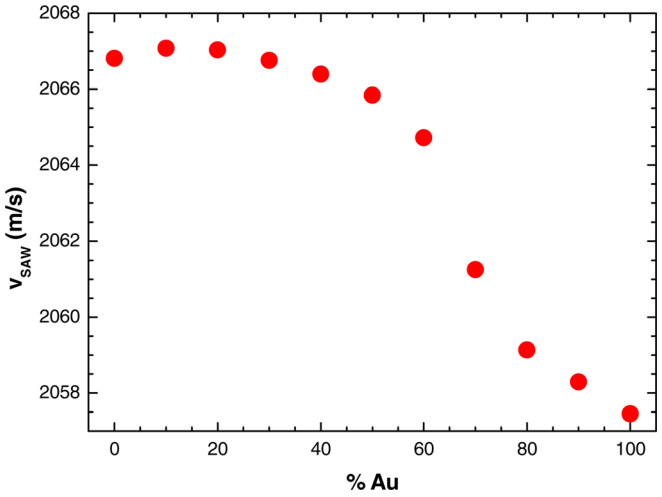

FIG. 8. (Color online) Variation of the mean value of the Rayleigh v_{SAW} with the increase of Au content in the native SiO_2 layer. The value at 100% must not be taken into account.

polycrystalline with the elastic constants of Table I. The SAW velocity value decreases by about 0.3% when Au/SiO_2 interlayer composition is varied from pure silica to pure gold material. Within the experimental error, and taking into account the existence of the interlayer, the sample grown at 450 K presents SAW velocity values typical of an ideal gold thin film on Si (001) substrate. This fact could be a sign for good adhesion to the substrate.

It has been well documented that, in defined circumstances, the deposition of Au films on Si substrates results in Au-Si mixtures, even alloys, known as gold silicides, with different degrees of crystallinity, depending, for instance, on the temperature treatments.[6–10] Probably, also Au diffusion within the native SiO_2 interlayer can play a role. Unfortunately, we cannot obtain direct information, neither about its composition nor their elastic properties, so the nature of the interlayer found remains unclear.

Finally, let us summarize the description of the observed variation in the SAW velocities of gold films on Si substrates when sputtering deposition is made at different temperatures. Elastic properties of samples deposited up to nearly 350 K are influenced by the small crystalline size (specifically at the "in-plane" directions), forming the Au thin film, which gives a diminution of the SAW velocities in respect to the values provided by the theory of the elasticity; this being due to the fact that small grains give a large density of grain boundaries, thus modifying the macroscopic elastic behavior. For temperatures well above room temperature, the morphology and microstructure improve as well as the elastic properties of the Au thin films, as shown by the SAW velocities for samples grown at 400 K and 450 K. The existence of an interlayer other than the native SiO_2 can be a sign for an improvement in the adhesion properties of the Au films on Si (001) substrates.

IV. CONCLUSIONS

Gold thin films have been deposited on Si (001) substrates by DC magnetron sputtering at different substrate temperatures. HRBS shows an increasing dependence of the SAW propagation velocity (Rayleigh mode) with deposition temperature.

Almost ideal elastic constant values are obtained for the sample grown at 450 K. The information obtained from x ray reflectivity for samples prepared above 300 K clearly shows the appearance of an interlayer of about 3 nm thickness that cannot be native SiO_2. This interlayer may be formed by diffusion of Au in the native SiO_2, but also the possibility that it may be formed by Au-Si alloys cannot be ruled out. Unfortunately, no information of its actual composition or its amorphous or crystalline character has been obtained. Moreover, the existence of this interlayer could be also interpreted as a sign of better adhesion of the Gold thin film on the Si substrate.

ACKNOWLEDGMENTS

This work has been supported by the Spanish Ministry of Science and Innovation under contract number MAT2009-08786. We wish to thank Dr. Carmen Munuera for her help in the AFM experiments. One of the authors (E. Salas) was supported with a Ph.D. Grant of the Spanish Ministry of Science and Innovation under ref. BES-2007-16745.

APPENDIX

We have used two different approaches to calculate the Voigt (V) and Reuss (R) ⟨111⟩ texture averaged elastic constants of gold: the one conducted in terms of the Voigt abbreviated subscript notation and exploiting an approach described by Auld[39] for transforming the 6×6 matrix elastic stiffnesses C_{IJ} and compliances S_{IJ}, and the other based on transformations of the fourth rank elastic stiffness and compliance tensors c_{ijkl} and s_{ijkl}, respectively. The latter approach entailed inter-conversion between the matrix and tensor elastic constants using the Voigt convention.[41] The numerical results that the two approaches yield are in precise agreement, as they should be. It is informative to briefly summarize these two approaches here. Our starting point is the published cubic crystal elastic stiffness matrix C_{IJ} of gold listed in Table I, from which we have obtained the compliance matrix S_{IJ} by matrix inversion and, in turn, established the tensors c_{ijkl} and s_{ijkl}. We have then rotated the x_3 axis into the ⟨111⟩ direction and x_1 into the $<-100>$ direction using the rotation matrix

$$\mathrm{a} = \begin{pmatrix} -1/\sqrt{2} & 1/\sqrt{2} & 0 \\ -1/\sqrt{6} & -1/\sqrt{6} & 2/\sqrt{6} \\ 1/\sqrt{3} & 1/\sqrt{3} & 1/\sqrt{3} \end{pmatrix}. \quad \text{(A1)}$$

In this rotated frame, the elastic stiffness and compliance tensors are respectively given by

$$c'_{ijkl} = a_{ip}a_{jq}a_{kr}a_{ls}c_{pqrs}, \quad s'_{ijkl} = a_{ip}a_{jq}a_{kr}a_{ls}s_{pqrs}, \quad \text{(A2)}$$

and the stiffness and compliance matrices are

$$C'_{IJ} = M_{IP}M_{JQ}C_{PQ} = \begin{pmatrix} 213.5 & 147.83 & 138.667 & 12.96 & 0 & 0 \\ 147.83 & 213.5 & 138.667 & -12.96 & 0 & 0 \\ 138.667 & 138.667 & 222.667 & 0 & 0 & 0 \\ 12.96 & -12.96 & 0 & 23.667 & 0 & 0 \\ 0 & 0 & 0 & 0 & 23.667 & 12.96 \\ 0 & 0 & 0 & 0 & 12.96 & 32.83 \end{pmatrix}, \tag{A3}$$

$$S'_{IJ} = N_{IP}N_{JQ}S_{PQ} = \begin{pmatrix} 0.0123662 & -0.00706459 & -0.00330159 & -0.0106434 & 0 & 0 \\ -0.00706459 & 0.0123662 & -0.00330159 & 0.0106434 & 0 & 0 \\ -0.00330159 & -0.00330159 & 0.00860317 & 0 & 0 & 0 \\ -0.0106434 & 0.0106434 & 0 & 0.0539135 & 0 & 0 \\ 0 & 0 & 0 & 0 & 0.0539135 & -0.0212867 \\ 0 & 0 & 0 & 0 & -0.0212867 & 0.0388615 \end{pmatrix}. \tag{A4}$$

In deriving the numerical results (which are in GPa and GPa^{-1}, respectively), expressions for the transformation matrices $\boldsymbol{M}$ and $\boldsymbol{N}$ in terms of $\boldsymbol{a}$, as provided by Auld[38] have been used. Note that, in this coordinate frame, the stiffness and compliance matrices display the form pertaining to trigonal $R1$ symmetry; in particular,

$$\begin{aligned} &C_{66} = \frac{1}{2}(C_{11} - C_{12}), S_{66} = 2(S_{11} - S_{12}), \\ &C_{14} = -C_{24} = C_{56}, S_{14} = -S_{24} = \frac{1}{2}S_{56}. \end{aligned} \tag{A5}$$

In view of the fact that there is no preferred orientation of the x_1 and x_2 axes in the plane perpendicular to x_3, this has now to be followed by an averaging of the elastic matrices and tensors over rotations of around the x_3 axis through a large number of regularly spaced angles Φ_n between 0 and 2π, using the rotation matrix

$$\mathrm{a} = \begin{pmatrix} \cos\Phi_n & \sin\Phi_n & 0 \\ -\sin\Phi_n & \cos\Phi_n & 0 \\ 0 & 0 & 1 \end{pmatrix}. \tag{A6}$$

The Voigt averaged stiffnesses are

$$C^V_{IJ} = \frac{1}{N}\sum_{n=1}^{N} C^{(n)}_{IJ}(\Phi_n), c^V_{Iijkl} = \frac{1}{N}\sum_{n=1}^{N} c^{(n)}_{ijkl}(\Phi_n). \tag{A7}$$

Performing the averaging either on the matrices or the tensors, we obtain the same numerical result

$$C^V_{IJ} = \begin{pmatrix} 213.5 & 147.83 & 138.667 & 0 & 0 & 0 \\ 147.83 & 213.5 & 138.667 & 0 & 0 & 0 \\ 138.667 & 138.667 & 222.667 & 0 & 0 & 0 \\ 0 & 0 & 0 & 23.667 & 0 & 0 \\ 0 & 0 & 0 & 0 & 23.667 & 0 \\ 0 & 0 & 0 & 0 & 0 & 32.83 \end{pmatrix}. \tag{A8}$$

As it can be seen, the Voigt averaging results only in the disappearance of C_{14} and its related constants from the stiffness matrix, leaving all other elements of the matrix unaltered. The stiffness matrix now displays the form pertaining to transverse isotropy or hexagonal symmetry.

The Reuss averaged compliances are

$$S^R_{IJ} = \frac{1}{N}\sum_{n=1}^{N} S^{(n)}_{IJ}(\Phi_n), s^R_{Iijkl} = \frac{1}{N}\sum_{n=1}^{N} s^{(n)}_{ijkl}(\Phi_n), \tag{A9}$$

and the Reuss stiffnesses are then obtained by matrix inversion, i.e.,

$$C^R_{IJ} = \left[S^R_{IJ}\right]^{-1}. \tag{A10}$$

Again, the same numerical results are obtained regardless of whether the averaging is performed over the compliance matrices or tensors, and the resulting Reuss stiffness matrix is

$$C^R_{IJ} = \begin{pmatrix} 206.399 & 154.934 & 138.667 & 0 & 0 & 0 \\ 154.934 & 206.399 & 138.667 & 0 & 0 & 0 \\ 138.667 & 138.667 & 222.667 & 0 & 0 & 0 \\ 0 & 0 & 0 & 18.548 & 0 & 0 \\ 0 & 0 & 0 & 0 & 18.548 & 0 \\ 0 & 0 & 0 & 0 & 0 & 25.732 \end{pmatrix}, \tag{A11}$$

displaying the form pertaining to transverse isotropy. It is interesting to observe that the values of the elastic constants C_{13} and C_{33} are independent of the type of averaging. This seems logical, as the rotating axis is the <001> axis of the trigonal symmetry. This result has previously been noted by ref. 40.

The Hill elastic stiffness matrix is obtained by averaging the Voigt and Reuss stiffness matrices, i.e.,

$$C_{IJ}^{VRH} = \frac{1}{2}C_{IJ}^{V} + \frac{1}{2}C_{IJ}^{R} = \begin{pmatrix} 209.95 & 151.38 & 138.667 & 0 & 0 & 0 \\ 151.38 & 209.95 & 138.667 & 0 & 0 & 0 \\ 138.667 & 138.667 & 222.667 & 0 & 0 & 0 \\ 0 & 0 & 0 & 21.11 & 0 & 0 \\ 0 & 0 & 0 & 0 & 21.11 & 0 \\ 0 & 0 & 0 & 0 & 0 & 29.28 \end{pmatrix}. \quad \text{(A12)}$$

This elastic constant matrix is the one used in the numerical simulations presented in Fig. 6.

[1] S. van Dijken, X. Fain, S. M. Watts, K. Nakajima, and J. M. D. Coey, J. Magn. Magn. Mater. **280**, 322 (2004).
[2] S. W. Han, H. W. Lee, H. J. Lee, J. Y. Kim, J. H. Kim, C. S. Oh, and S. H. Choa, Curr. Appl. Phys. **6S1**, e81 (2006).
[3] Y. Yamazaki, Electrochim. Acta **50**, 663 (2004).
[4] C. Wang and M. Madou, Biosens. Bioelectron. **20**, 2181 (2005).
[5] S. Kal, A. Bagolini, B. Margesin, and M. Zen, Microelectron. J. **37**, 1329 (2006).
[6] Z. Ma and L. H. Allen, Phys. Rev. B **48**, 15484 (1993).
[7] J. Biskupek, U. Kaiser, and F. Falk, J. Electron Microsc. **57**, 83 (2008).
[8] C. L. Kuo and P. Clancy, Surf. Sci. **551**, 39 (2004).
[9] A. G. Ramirez and R. Saha, Appl. Phys. Lett. **85**, 5215 (2004).
[10] J. Alonso, M. L. Fdez-Gubienda, G. Sarmiento, J. M. Barandiarán, A. Svalov, I. Orue, J. Chaboy, L. Fernández Barquín, C. Meneghini, T. Neisius, and N. Nawamura, Appl. Phys. Lett. **95**, 082103 (2009).
[11] E. Irissou, B. Le Drogoff, M. Chaker, M. Trudeau, and D. Guay, J. Mater. Res. **19**, 950 (2004).
[12] Bhuvana and G. U. Kulkarni, Bull. Mater. Sci. **29**, 505 (2006).
[13] C. V. Thompson and R. Carel, J. Mech. Phys. Solids **44**, 657 (1996).
[14] M. Dietiker, S. Olliges, M. Schinhammer, M. Seita, and R. Spolenak, Acta Mater. **57**, 4009 (2009).
[15] M. T. Lin, R. R. Chromik, N. Barbosa III, P. El-Deiry, S. Hyun, W. L. Brown, R. P. Vinci, and T. J. Delph, Thin Solid Films **515**, 7919 (2007).
[16] B. Hildebrands, P. Baumgart, R. Mock, G. Güntherodt, and P. S. Bechthold, J. Appl. Phys. **58**, 3166 (1985).
[17] M. Grimsditch, R. Bhadra, and I. K. Schuller, Phys. Rev. Lett. **58**, 1216 (1987).
[18] D. Faurie, P. O. Renault, E. Le Bourhis, and Ph. Godeau, Acta Mater. **54**, 4503 (2006).
[19] M. G. Beghi, C. E. Bottani, L. Guzman, T. Lafford, N. Laidani, P. M. Ossi, and B. K. Tanner, Thin Solid Films **317**, 198 (1998).
[20] E. Salas, R. J. Jiménez-Riobóo, A. de Andrés, and C. Prieto, Eur. Phys. J. B **75**, 151 (2010).
[21] F. Jiménez-Villacorta, A. Muñoz-Martín, R. Ramírez, and C. Prieto, Mater. Sci. Eng., C **26**, 1141 (2006).
[22] H. D. Espinosa and B. C. Prorok, J. Mater. Sci. **38**, 4125 (2003).
[23] E. Salas, R. J. Jiménez Riobóo, A. Muñoz-Martín, and C. Prieto, IOP Conf. Ser.: Mater. Sci. Eng. **12**, 012014 (2010).
[24] T. F. Young, J. F. Chang, and H. Y. Ueng, Thin Solid Films **322**, 319 (1998).
[25] H. Tanimoto, Y. Koda, S. Sakai, H. Mizubayashi, and E. Kita, Scr. Mater. **44**, 2231 (2001).
[26] E. Seker, J. T. Gaskins, H. Bart-Smith, J. Zhu, M. L. Reed, G. Zangari, R. Kelly, and M. R. Begley, Acta Mater. **55**, 4593 (2007).
[27] C. R. Chen and L. J. Chen, Appl. Surf. Sci. **92**, 507 (1996).
[28] M. G. Beghi, C. E. Bottani, P. M. Ossi, T. A. Lafford, and B. K. Tanner, J. Appl. Phys. **81**, 672 (1997).
[29] I. Horcas, R. Fernández, J. M. Gómez-Rodríguez, J. Colchero, J. Gómez-Herrero, and A. Baro, Rev. Sci. Instrum. **78**, 013705 (2007).
[30] J. K. Krüger, "Brillouin spectroscopy and its application to polymers" in *Optical Techniques to Characterize Polymer Systems*, edited by A. Bässler (Elsevier, Amsterdam, 1989).
[31] R. J. Jiménez-Riobóo, M. García-Hernández, C. Prieto, J. J. Fuentes-Gallego, E. Blanco, and R. Ramírez del Solar, J. Appl. Phys. **81**, 7739 (1997).
[32] J. R. Sandercock, in *Light Scattering in Solids III* (Springer-Verlag, Berlin, 1982).
[33] P. Mutti, C. E. Bottani, G. Ghislotti, M. Beghi, G. A. D. Briggs, and J. R. Sandercock, *Advances in Acoustic Microscopy* (Plenum, New York, 1995), Vol. 1, p. 249.
[34] X. Zhang, J. D. Comins, A. G. Every, P. R. Stoddart, W. Pang, and T. E. Derry, Phys. Rev. B **58**, 13667 (1998).
[35] F. Jiménez-Villacorta, A. Muñoz-Martín, and C. Prieto, J. Appl. Phys. **96**, 6224 (2004).
[36] A. Muñoz-Martín, "Caracterización estructural de sistemas magnéticos nanoestructurados," PhD thesis (Universidad Autónoma de Madrid and Consejo Superior de Investigaciones Científicas, 2002).
[37] B. C. Hendrix and L. G. Yu, Acta Mater. **46**, 127 (1998).
[38] L. Bassoli, F. Nizzoli, and J. R. Sandercock, Phys. Rev. B **34**, 1296 (1986).
[39] B. A. Auld, in *Acoustic Fields and Waves in Solids* (Krieger, Florida, 1990), Vol. 1.
[40] D. R. Lide, in *CRC Handbook of Chemistry and Physics*, 82nd ed. (CRC, London, 2001), Chap. 14, p. 38.
[41] A. G. Every, "The elastic properties of solids: Static and dynamic principles" in *Handbook of Elastic Properties of Solids, Liquids and Gases*, edited by M. Levy, H. E. Bass, and R. R. Stern (Academic, San Diego, 2001), Vol. 1, Chap. 1.